JGR Atmospheres

RESEARCH ARTICLE
10.1029/2022JD038322

The Role of Stratified Turbulence in the Cold Summer Mesopause Region

Victor Avsarkisov[1,2] and J. Federico Conte[3]

[1]Department of Modelling of Atmospheric Processes, Leibniz Institute of Atmospheric Physics at the University of Rostock, Kühlungsborn, Germany, [2]Now at Meteorological Institute, Universität Hamburg, Hamburg, Germany, [3]Department of Radar Remote Sensing, Leibniz Institute of Atmospheric Physics at the University of Rostock, Kühlungsborn, Germany

Key Points:

- Spatially filtered horizontal wind residuals are explored for the first time at mesopause altitudes over Patagonia
- Frequency spectra of horizontal wind residuals follow a −2 slope
- Simulated divergent and rotational parts of the mesoscale kinetic energy are equipartitioned at high frequencies

Correspondence to:

V. Avsarkisov and J. F. Conte,
victor.avsarkisov@uni-hamburg.de;
conte@iap-kborn.de

Citation:

Avsarkisov, V., & Conte, J. F. (2023). The role of stratified turbulence in the cold summer mesopause region. *Journal of Geophysical Research: Atmospheres*, *128*, e2022JD038322. https://doi.org/10.1029/2022JD038322

Received 7 DEC 2022
Accepted 26 AUG 2023

Author Contributions:

Conceptualization: Victor Avsarkisov, J. Federico Conte
Formal analysis: Victor Avsarkisov, J. Federico Conte
Investigation: Victor Avsarkisov, J. Federico Conte
Methodology: Victor Avsarkisov, J. Federico Conte
Software: Victor Avsarkisov, J. Federico Conte
Writing – original draft: Victor Avsarkisov, J. Federico Conte
Writing – review & editing: Victor Avsarkisov, J. Federico Conte

Abstract The summer mesopause at middle and high latitudes is the coldest place on Earth, and atmospheric gravity waves are responsible for the emergence of this extreme thermal phenomenon. Although the main physical mechanism behind the latter is understood, a deeper insight into it can be gained from the investigation of the mesoscale energy spectrum. In this work, we decompose the frequency spectra into divergent and rotational parts and find that their energy contributions are equipartitioned at high frequencies. This mesoscale energy equipartition is a feature of stratified turbulence and illustrates the complexity of the mesoscale dynamics in the summer mesopause region. We also analyze the power spectra of observed and simulated mesoscale zonal and meridional winds at middle latitudes in the Southern Hemisphere and show that stratified turbulence plays a role in the mesopause region during summer.

Plain Language Summary Given its complexity to be measured at different spatio-temporal scales, the exploration of the mesosphere and lower thermosphere remains an active area of research. In this work, we have applied velocity filtering techniques to both multistatic specular meteor radar measurements and global circulation model simulations to analyze horizontal wind frequency spectra over southern Patagonia. We consider the theory of layered anisotropic stratified turbulence to study the summer mesopause region and hypothesize that this type of turbulence (in the statistical sense) plays a role in the transition of internal gravity waves to small-scale turbulence.

1. Introduction

The vertical structure of the terrestrial atmosphere consists of different layers. The troposphere and lower stratosphere build the lower atmosphere, which is a dynamically active region where most of the gravity wave (GW) generation takes place. In the middle atmosphere, which spans from the lower stratosphere up to ∼110 km of altitude, the complex mesoscale dynamics induce some of the most fascinating atmospheric phenomena. One of them is the presence of noctilucent clouds (NLCs), which are formed by small ice particles at altitudes of 80–85 km during the summer at middle and high latitudes. NLCs are a consequence of mesoscale GW breaking (Lindzen, 1981), a process that cools the summer mesopause region down to ∼130 K (−143°C), making it the coldest place on Earth (Lübken, 1999; McIntyre, 2000), and thus allowing the formation of these ice particles.

Although the mechanism responsible for the cold summer mesopause is understood, a deeper insight into this phenomenon can be gained from the analysis of the mesoscale energy spectrum. Such analysis is complex, mainly because of the limited amount of mesoscale observations and simulations currently available. Another difficulty lies in the interpretation of the mesospheric signals. Until now, two competing theories have been used to explain the observed mesoscale dynamics in the upper troposphere and lower stratosphere (UTLS) region, which can also explain similar dynamics in the mesosphere (Avsarkisov et al., 2022). One of them considers GWs as the main mechanism driving the dynamics (Dewan, 1979). The other theory uses two-dimensional turbulence to explain the observed variability (Gage, 1979; Lilly, 1983). Advancements in measurement techniques presented by Nastrom and Gage (1985) allowed to measure horizontal winds and temperatures at high resolutions. The result of this seminal study was the construction of the wavenumber spectra of the temperature and velocity components in the UTLS, and the confirmation that synoptic-scale and mesoscale dynamics have scaling behaviors of k^{-3} and $k^{-5/3}$, respectively (k being the horizontal wavenumber). The classical theory of two-dimensional turbulence predicted an inverse energy cascade for these mesoscales (Falkovich, 1992; Gage, 1979), while the GW theory employed weakly nonlinear inertia-GWs to explain a downscale mesoscale cascade (Dewan, 1979;

VanZandt, 1982). The cascade direction was analyzed by Lindborg (1999). He used third-order longitudinal structure-functions applied to the measurements from Nastrom and Gage (1985) and concluded that the mesoscale energy cascades toward small scales.

Thus, a new turbulence theory was required to explain the $k^{-5/3}$ mesoscale range. That theory is layered anisotropic stratified turbulence, or LAST (Caulfield, 2020, 2021; Falder et al., 2016), formulated in the studies by Billant and Chomaz (2001), Lindborg (2006), and Smyth and Moum (2000). This theory allows forward energy cascade in vertically anisotropic and three-dimensional turbulent flows, and explains the mesoscale part of the Nastrom-Gage spectrum as a superposition of GWs and layered coherent vortical pancake-like structures.

Currently, the two aforementioned theories, namely, weakly nonlinear GWs (Callies et al., 2014; Dewan, 1979) and strongly nonlinear LAST are used to explain atmospheric mesoscale dynamics. Until recently, the similarity in the predictions by both theories of the horizontal wavenumber energy spectrum made it impossible to determine the dominant mesoscale process without a velocity field decomposition into divergent and rotational (or vortical) parts.

The frequency spectra of GWs have been measured and analyzed in multiple studies. Based on their results, it is accepted that the spectral slope varies from -1.4 to -2 and usually falls as $-5/3$ irrespective of altitudes, latitudes, or seasons (e.g., Weinstock, 1996). This observational evidence suggests the presence of a global source in the lower atmosphere that generates most of the upward propagating GWs. Various studies attribute this universality of the observed GW spectra to different mechanisms, such as off-resonant wave-wave interactions (Gardner, 1994), convective or dynamical instabilities of saturated GWs (Dewan & Good, 1986; Smith et al., 1987), or to nonlinear interactions (Weinstock, 1990). Currently, the idea of the presence of a global GW source is realized in multiple GW drag parameterization schemes. This source should be present around the globe and should be associated with the coupling between synoptic-scale waves and geostrophic turbulence. Recently, it has been found that the frequency spectra become shallower at 60–65 km (~ -1.4) than in the stratosphere (~ -1.8 to -2.0) (Zhao et al., 2017).

In the present study, we employ a combination of novel multistatic specular meteor radar (SMR) measurements and high-resolution model simulations to investigate the frequency power spectra of mesoscale horizontal winds and, thus, determine the relative importance of weakly nonlinear GWs and strongly nonlinear LAST regimes at mesopause altitudes during the summer. The paper is structured as follows. Section 2 describes the methods applied to the multistatic SMR observations and the model simulations to extract information about mesoscale horizontal winds. Section 3 is used to present and discuss the main results of this work, and Section 4 is reserved for the conclusions of this study.

2. Data Analysis

2.1. Multistatic Specular Meteor Radar Observations

As observational basis, Doppler shift measurements provided by Spread spectrum Interferometric Multistatic meteor radar Observing Network (SIMONe) Argentina have been used to estimate horizontal wind residuals between 82 and 96 km of altitude. SIMONe Argentina is a state-of-the-art multistatic SMR network deployed in the region close to El Calafate, in Argentine Patagonia. It is comprised of one five-antenna transmitting site, and five single-antenna receiving sites located within a radius of ∼250 km around the transmitter, which situates at 49.6°S, 71.4°W. More details of SIMONe Argentina can be found in Chau et al. (2021) and Conte et al. (2021).

To obtain information on the mesosphere and lower thermosphere mesoscale dynamics, spatially filtered horizontal wind residuals were calculated by subtracting two different estimates of the mean wind vector. In both wind estimations, the following equation was solved in bins of 30 min and 2 km, shifted by 15 min and 1 km, respectively,

$$\mathbf{u} \cdot \mathbf{k} = 2\pi f + \epsilon. \tag{1}$$

Here, $\mathbf{k}$ is the Bragg wave vector (scattered minus incident vectors), determined taking into consideration the World Geodetic System 1984 (e.g., Chau & Clahsen, 2019); f and ϵ are the Doppler shift and its measurement error; and $\mathbf{u} = (u, v, w)$ is the wind vector in the meteor-centered east-north-up frame of reference. To retrieve the zonal (u) and meridional (v) wind components, Equation 1 was solved by means of a weighted least squares

method applied to the time-altitude bins containing a minimum of 10 meteor detections. The inverse of the squared Doppler errors were used as weights.

The distinction between the two wind estimations lies in the horizontal area taken into consideration to solve Equation 1. The first wind estimates were calculated considering the meteors detected within a horizontal area of 80 km of radius around a selected reference point. The reference point has latitude and longitude identical to those of the transmitting site, and a height equal to the altitude at which Equation 1 is solved. The second wind estimation was carried out using all the meteors detected within a horizontal area of 200 km radius around the same reference point. In both cases, only the meteor detections with corresponding zenith angles smaller than 60° were used.

The horizontal winds estimated using an area of 200 km radius represent the mean value of all the irregularities with horizontal scales larger than 400 km. This is because the variability that develops in horizontal scales smaller than 400 km is averaged out by the estimation procedure. Similarly, the horizontal winds estimated considering the meteors detected within an area of 80 km radius represent a mean value of those irregularities with horizontal scales larger than 160 km. Consequently, the difference between the 160 km and the 400 km mean winds is driven by irregularities with horizontal scales in the range of 160–400 km. Subtracting a 400 km mean value may not perfectly remove all irregularities with horizontal scales larger than 400 km. Thus, a 3 hr running mean was also subtracted in order to finally obtain the so-called spatially filtered wind residuals, hereafter referred as $(\mathbf{u}_{160\text{km}} - \mathbf{u}_{400\text{km}})$.

The spectra of the wind residuals were calculated using the Fast Fourier Transform (FFT) with a Hanning (or Cosine Bell) window. The procedure was applied to 1 week of spatially filtered wind residuals estimated at 90 km of altitude.

2.2. Model Simulations

In this study, we have analyzed simulation results from the Kühlungsborn Mechanistic Circulation Model (KMCM). The KMCM is based on a spectral dynamical core and solves the primitive equations with a terrain-following vertical hybrid coordinate (Simmons & Burridge, 1981). The model extends from the surface to the lower thermosphere (1.5×10^{-5} hPa, $z \sim 140$ km) using 190 full model layers. The level spacing is about 600 m between the boundary layer and the mesopause region, and becomes coarser at higher altitudes. The KMCM employs a triangular spectral truncation at a total horizontal wavenumber of 240 (T240), which corresponds to the shortest resolved horizontal wavelength equal to 165 km, or a horizonal grid spacing of 55 km. This model version, abbreviated as T240L190, is well documented and has been applied in several previous studies (e.g., Avsarkisov et al., 2022; Becker & Vadas, 2018, 2020; Vadas & Becker, 2018). In this work, we used the simulation data from these previous studies.

The KMCM is a free-running, GW resolving model. Unresolved scales are parameterized by a Smagorinsky scheme for vertical and horizontal diffusion that is extended by a weak hyperdiffusion (Becker, 2009; Brune & Becker, 2013).

The present study aims to analyze the frequency spectra of zonal and meridional velocities in the mesopause region in the same volume as the SIMONe Argentina system. To do so, we post-processed 15 days of KMCM simulations at three given locations (47°S, 72°W; 49°S, 72°W; and 51°S, 72°W) performed with Southern Hemisphere's summer conditions without nudging. First, we controlled that the simulation results obtained for these three locations with similar orography were statistically stationary. Then, the wind fields obtained at these three locations were averaged into a single time series with a 22.5 min temporal resolution for further investigation. Before the analysis of the frequency spectra, the data was split into three 5-day segments. The frequency spectrum of each time interval was calculated using the FFT with a Hanning window, similarly to the meteor radar data procedure. Finally, the obtained three spectra were averaged to obtain one single smoother spectrum for each horizontal wind component.

The KMCM allows to calculate horizontal winds in the form of spectral amplitudes for the horizontal divergence and vorticity (Brune & Becker, 2013). This wind decomposition technique proved to be extremely useful in removing the large-scale geostrophically balanced flow from the real-time dynamics (Becker, 2012). In the present study, we combine this wind decomposition method with a second filtering technique to obtain the mesoscale

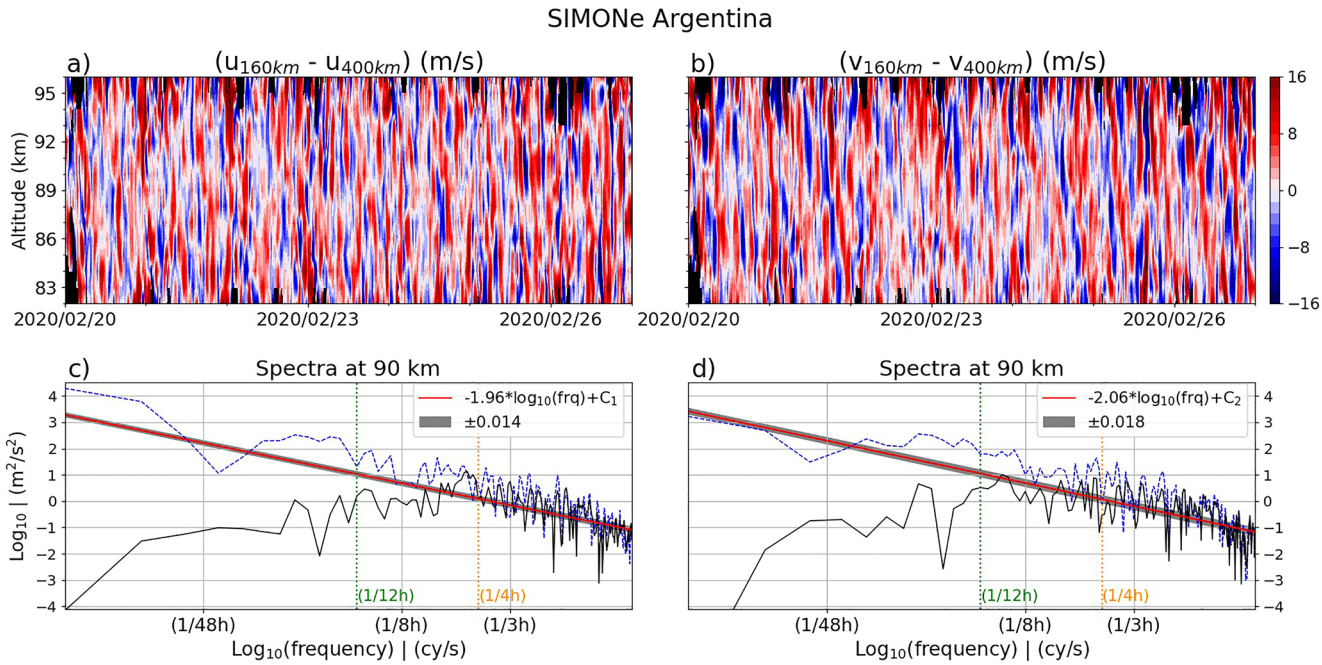

Figure 1. The upper panels show (a) zonal and (b) meridional wind residuals estimated from SIMONe Argentina measurements obtained between 20 February and 27 February 2020 (data gaps are indicated in black). The bottom panels (c, d) show the corresponding frequency power spectra at 90 km of altitude. The spectra of the wind residuals are indicated in black, while the dashed blue curves depict the spectra of the 160 km mean winds. In red, the straight line that best fits the black curve for periods shorter than 8 hr is presented. The shaded gray area indicates the error in the slope estimate.

parts of the horizontal divergence and vorticity. The second filtering technique used in this study employs the spectral properties of the code. The method allows the calculation of the horizontal mesoscale winds from the full spectral expansion (up to wavenumber 240) by subtracting the synoptic-scale winds, represented by the first 40 wavenumbers (this corresponds to 1,000 km scales) (Avsarkisov et al., 2022; Becker, 2009). To match the simulated results with the observational data, we modified our spectral filtering technique and subtracted the first 100 wavenumbers (this corresponds to 400 km scales). Both filtering techniques are applied simultaneously and facilitate the decomposition of both zonal and meridional components of the horizontal wind into the following four parts: the balanced geostrophic flow components (U_g, V_g) with L_x, $L_y > 400$ km, the synoptic-scale waves and GW components (U_w, V_w) with L_x, $L_y > 400$ km, the mesoscale vortical components (u_{rot}, v_{rot}) with 165 km $< L_x$, $L_y < 400$ km, and the mesoscale GW components (u_{div}, v_{div}) with 165 km $< L_x$, $L_y < 400$ km. L_x and L_y are the zonal and meridional wavelengths.

3. Results and Discussion

In Figure 1, panels (a) and (b), seven days of zonal ($u_{160\mathrm{km}} - u_{400\mathrm{km}}$) and meridional ($v_{160\mathrm{km}} - v_{400\mathrm{km}}$) wind residuals obtained from SIMONe Argentina are respectively presented as a function of time and altitude. These two parameters were estimated following the procedure described in Section 2.1. Notice that significant variability in time and altitude is seen in both components. This variability is driven by irregularities that extend over horizontal areas not larger than 400 km. The vertical scales are in the order of 2 km or more. The amplitudes are around ±8 m/s, sometimes exceeding absolute values of 10–12 m/s. Data gaps are indicated in black.

The lower left (c) and right (d) panels are used to present the frequency power spectra of the zonal and meridional wind residuals, respectively. The latter are indicated with the continuous black curves. The straight line that best fits the part of the spectra that corresponds to periods shorter than 8 hr is shown in red. The value of 8 hr was arbitrarily selected. The shaded gray area indicates the error in the slope estimate. The blue dashed curves correspond to the spectra of the 160 km mean horizontal winds ($u_{160\mathrm{km}}$ and $v_{160\mathrm{km}}$). All spectra were calculated at 90 km because at this altitude level it was possible to find a complete week of data without any gaps, and thus avoid interpolating or zero-padding. The frequency power spectrum follows an almost −2 slope in both components of

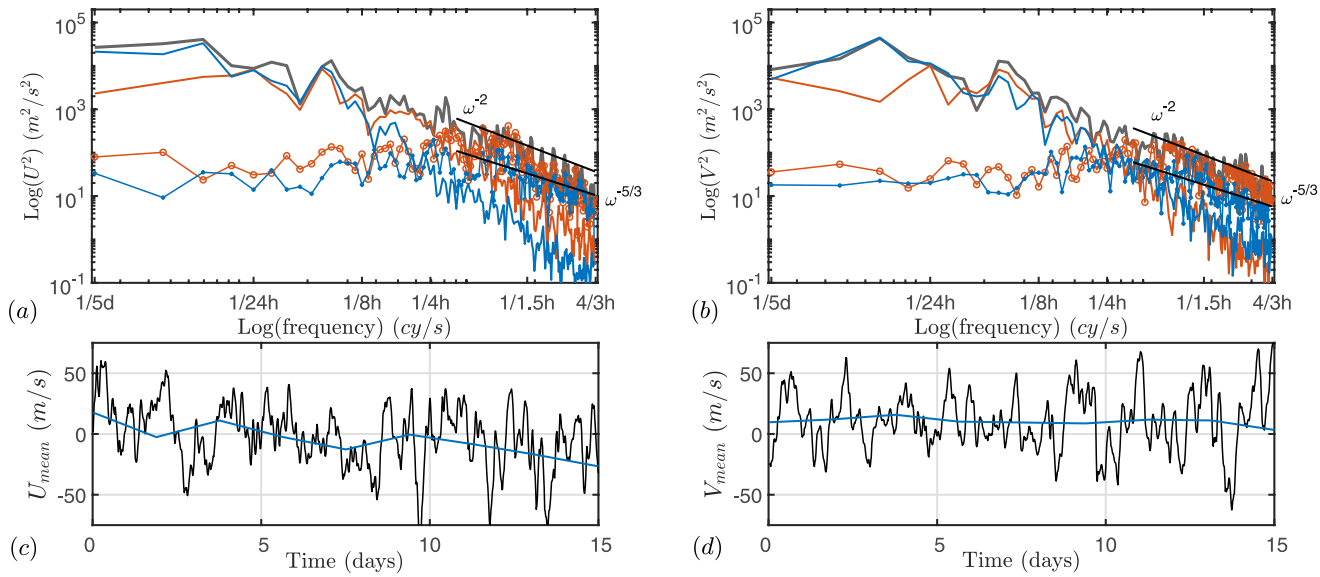

Figure 2. Panels (a) and (b) show the spectral decomposition of the total zonal and meridional wind field, respectively. The gray curve represents the total wind field. The orange curves correspond to the wind divergent fields (U_w, V_w, u_{div}, v_{div}), which are associated with waves. The blue curves correspond to wind rotational fields (U_g, V_g, u_{rot}, v_{rot}), which are associated with vortical structures. The solid orange and blue curves represent the large-scale waves (U_w, V_w) and balanced flow (U_g, V_g), respectively. The solid curves with markers correspond to mesoscale GWs (u_{div}, v_{div}) (orange circles) and vortical motions (u_{rot}, v_{rot}) (blue dots). The black solid straight lines highlight the ω^{-2} and $\omega^{-5/3}$ slopes. The mean background zonal ($U_{\mathrm{mean}} = U_w + U_g$) and meridional ($V_{\mathrm{mean}} = V_w + V_g$) winds are presented in panels (c) and (d), respectively. The black curves correspond to 45 min resolution background winds, and the blue curves represent the daily mean values.

the horizontal wind residuals (black curves). Notice that despite the fact that the filtering procedures applied to the data are not perfect; the energy contributions from irregularities with large periods have been significantly reduced. This can be better appreciated by comparing the spectra of the wind residuals with those of the 160 km mean winds (blue curves).

Thus, the main result of the observational part of our study is that the spatially filtered wind fluctuations with horizontal scales between 160 and 400 km have a −2 slope in the frequency domain. This observational result requires further investigation, and hence outputs from idealized GCM simulations with similar horizontal and temporal resolutions are explored in order to construct frequency spectra of wind fluctuations at the same altitudes and under the same seasonal conditions.

Figures 2a and 2b show the frequency power spectra of the zonal and meridional velocities extracted from KMCM. The solid orange and blue curves with markers (circles and dots) correspond to the divergent (u_{div}, v_{div}) and rotational (u_{rot}, v_{rot}) parts of the mesoscale velocities, representing GWs and vortical motions, respectively. The mesoscale GW component (orange circles) decreases with a −2 spectral slope in the subrange between 4 and 1 hr periods. This numerical result supports our observations at 90 km of altitude (see Figures 1c and 1d). This similarity in the slope between the simulated divergent part of the horizontal winds and the observational data sets suggests that the ω^{-2} power law is the generic feature of the mesoscale GW cascade in the cold summer mesopause region.

A predominance of the GW component (u_{div}, v_{div}) is visible in the simulated frequency spectra for periods varying from 4 hr down to 1.5 hr. However, the rotational part (u_{rot}, v_{rot}) of the mesoscale wind fluctuations becomes energized at periods of approximately 2 hr and follows a −5/3 spectral slope (see dotted blue curves in Figures 2a and 2b). This shallowing of the rotational part of the spectrum observed in our simulations is in accordance with the Eulerian frequency spectrum of isotropic turbulence (Tennekes, 1975). The relative spectral dominance of the rotational and divergent components exhibits an approximate equipartitioning at periods of 1 hr or less. While the ratio $R_v = v_{div}^2/v_{rot}^2$ decreases only slightly depending on the period ($R_v|_{75min>\omega^{-1}>1h} = 4.06$ and $R_v|_{1h>\omega^{-1}>45min} = 3.79$), the ratio $R_u = u_{div}^2/u_{rot}^2$ exhibits a clear decrease at high frequencies ($R_u|_{75min>\omega^{-1}>1h} = 1.90$ and $R_u|_{1h>\omega^{-1}>45min} = 1.17$).

This equipartition between the rotational and divergent components is one of the main spectral characteristics of the LAST regime, as it was formulated in the early studies by Lindborg (2006) and Riley and Lindborg (2013).

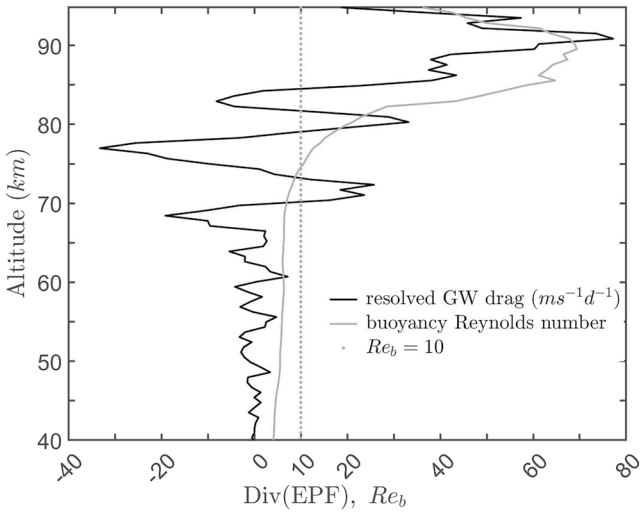

Figure 3. Altitudinal profiles of the mean over 30 days of January of the Eliassen-Palm flux (EPF) divergence from GWs with horizontal wavelengths shorter than ~400 km (solid black line), and the corresponding profile of the buoyancy Reynolds number Re_b, defined as $Re_b = \epsilon/(\nu N^2)$ (solid gray line). The dotted vertical line highlights the stratified turbulence existence condition $Re_b = 10$. The exact form of the EPF divergence is given in the appendix of Becker (2009).

The decrease of R_u and R_v at these scales indicates the growing importance of stratified turbulence and suggests the strongly nonlinear character of mesoscale dynamics at smaller unresolved horizontal scales. The equipartition of the rotational and divergent components also highlights the importance of the divergent component (GWs) for the LAST regime. The theory of LAST stems from a "*one fluid*" attitude (Holloway, 1988), that is, it assumes that GWs and vortical motions co-exist in the same flow volume. Thus, there is one joint field of velocity fluctuations and a single field of buoyancy fluctuations. This theory was already successfully used by the authors in other observational and numerical studies of the lower and middle atmosphere (Avsarkisov et al., 2022; Chau et al., 2020; Ghosh et al., 2022; Poblet et al., 2022, 2023).

The mean altitudinal profiles of the filtered resolved GW drag and the buoyancy Reynolds number in Figure 3 highlight the relative importance of the divergent and rotational energy parts for the LAST. The increase in the GW drag above 80 km of up to 75 ms^{-1} day^{-1} is associated with a similar behavior in Re_b. Thus, the breaking process of the primary GWs induces stratified turbulence in the cold summer mesopause region. The exact mechanism of how LAST affects the cold summer mesopause is currently missing. However, based on recent progress in the exploration of LAST (Caulfield, 2020, 2021), we expect to observe the following scenario in the summer extratropical mesopause region: the breaking of primary GWs in this region generates areas of locally well-mixed high-Reynolds number turbulence. These turbulent filaments get entrained by the strong stratification field and, under the influence of the background wind, spread in the horizontal direction to form pancake-like thin (layered) turbulent structures.

Inspection of the synoptic-scale part of the spectra presented in Figures 2a and 2b reveals that at periods from 5 days down to 24 hr, the large-scale balanced flow (solid blue) dominates the frequency spectrum (solid gray). Synoptic-scale waves and large-scale GWs (solid orange) dominate the spectrum at periods of less than 24 hr. At periods smaller than approximately 6 hr, the balanced flow (solid blue) exhibits a decrease with a steeper than ω^{-3} slope (close to ω^{-4}). At periods smaller than 4 hr, the divergent component (solid orange) exhibits the same steep slope. The steeper slope of the large-scale parts at high frequencies indicates a significant decrease in the importance of synoptic scales for mesoscale dynamics. This feature could eventually be used as a different approach for background wind identification. However, the physical interpretation of the peculiar, possibly ω^{-4} scaling behavior, will be the subject of future studies.

3.1. A Comment on the Validity of the Helmholtz-Hodge Decomposition

When the GWs intrinsic frequency and the inertial frequency are comparable, it is impossible to decompose the horizontal wind field into rotational and divergent parts, as the rotational part of these GWs is not zero (Koshyk et al., 1999; Liu, 2019). As it has been shown by Avsarkisov et al. (2022), this condition is valid for GWs with periods of approximately 8 hr or more, as the Rossby number for waves with shorter periods is equal to 1 at summer mesopause altitudes. In the present study, we focus on a comparison of the mesoscale rotational and divergent components of velocities at periods between 2 hr and 45 min. Thus, we assume that the vertical component of the vorticity of these high-frequency GWs is equal to zero and hence the rotational part can be associated solely with vortical motions.

3.2. The Theory of Layered Anisotropic Stratified Turbulence

The theory of LAST is characterized by two main non-dimensional parameters: the buoyancy Reynolds number, $Re_b = \epsilon/(\nu N^2)$, and the horizontal Froude number, $Fr_h = u_{h_{meso}}/(N l_h)$. The former parameter assures that the system has enough energy to initiate the isotropic cascade in the flow $\left(Re_b = (l_o/\eta)^{4/3} \gg 1\right)$, while the latter indicates the stratification rate of the flow: $Fr_h = l_v/l_h$ (Brethouwer et al., 2007). Here, $l_o = \sqrt{\epsilon/N^3}$ is the Ozmidov scale, $\eta = \left(\nu^3/\epsilon\right)^{1/4}$ is the Kolmogorov scale, $l_h = u^3_{h_{meso}}/\epsilon$ and $l_v \sim l_b = u_{h_{meso}}/N$ are the characteristic horizontal,

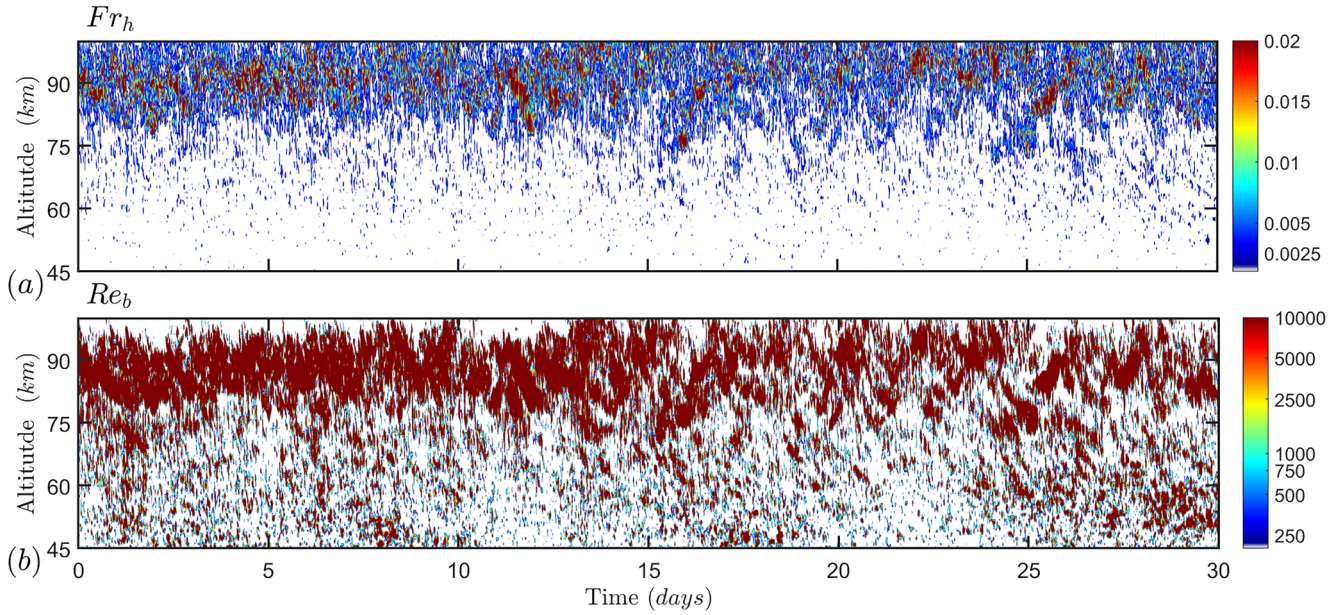

Figure 4. Impact of the stratified turbulence on the summer mesopause region. Panels (a) and (b) present the KMCM horizontal Froude number, $Fr_h = \epsilon / N u^2_{h_{meso}}$ and the buoyancy Reynolds number Re_b. It can be seen that the layered anisotropic stratified turbulence regime is present in the region between 80 and 95 km of altitude.

vertical and buoyancy scales (Billant & Chomaz, 2001); ϵ is the turbulent dissipation rate, ν is the kinematic viscosity, N is the Brunt-Väisälä frequency, and $u_{h_{meso}} = u_{div} + u_{rot}$ is the residual wind. An extensive review of the current development of the theory of LAST can be found in recently published books (Davidson, 2013; Riley & Lindborg, 2013) and reviews (Caulfield, 2020, 2021). Figure 4 provides the temporal evolution of the main non-dimensional parameters that govern stratified turbulence, namely, the horizontal Froude number and the buoyancy Reynolds number, calculated using the data from KMCM simulations. The peak of Re_b and Fr_h is located at 90 km altitude, as it was already highlighted in Avsarkisov et al. (2022).

4. Concluding Remarks

In this work, mesoscale dynamics have been investigated using novel filtering techniques applied to the observational data obtained from SIMONe Argentina and to simulated data extracted from KMCM. A spatial filtering method developed for the SIMONe Argentina system allows estimating horizontal wind residual components in scales of a few hundred kilometres, whose frequency spectra follow a -2 slope. A spectral filtering method applied to the simulated data and a feature of spherical harmonics to describe the simulated wind field as a sum of rotational and divergent components allowed us to decompose the horizontal wind residuals into rotational and divergent components. Due to the little effect of Coriolis force at these residual scales (less than 400 km), the mesoscale divergence is associated with internal GWs, while the rotational component is linked only to vortical motions.

Our spectral filtering reveals that a considerable part of the residual mesoscale kinetic energy is concentrated in the rotational component of the horizontal winds. Due to the reasons mentioned above, this rotational component cannot be associated with internal GWs at these scales. Hence, there is a type of vortical (or rotational) motion that contains this energy and is strongly affected by stratification. In this sense, we show that the rotational and divergent parts of the kinetic energy are equal at the smallest resolved temporal scales, which represent horizontal scales in the order of 150–200 km. The latter is a well-known characteristic of the LAST regime (Li & Lindborg, 2018; Lindborg, 2006).

The quantitative presentation of the GW drag, and the buoyancy Reynolds number profiles highlights the mechanism of turbulence generation due to GW breaking. In other words, there is a significant downward cascade of the mesoscale energy in the summer mesopause region.

Concerning the specific (Fr_h, Re_b) parameter space regime (Brethouwer et al., 2007; Lindborg, 2006), the low horizontal Froude numbers ($Fr_h < 0.02$) and high buoyancy Reynolds numbers ($Re_b > 10$) suggest strong (stable) stratification and high turbulization of the atmosphere in the region between 85 and 90 km.

The combination of the above three (rot-div energy equipartition, downward cascade, and the results of the parameter space study) creates a clear picture of the mesoscale dynamics in the summer mesopause region. It favors the stratified turbulence approach over the standard GW theory at temporal scales below 1 hr. Thus, the transition of mesoscale GWs to vortical motions can be described by the scaling laws of the LAST in the statistical sense.

Data Availability Statement

The SIMONe Argentina data and KMCM outputs used to produce the figures of this paper are publicly available at https://doi.org/10.22000/1737.

Acknowledgments
V.A. acknowledges support of his research by the Leibniz Society (Germany) via the SAW project FORMOSA. The work of J.F.C. was partially supported by the Bundesministerium für Bildung und Forschung (Germany), via project WASCLIM-IAP, part of the ROMIC-II program. The authors thank Erich Becker for providing the KMCM code and a critical reading of the manuscript. The authors thank Matthias Clahsen and Nico Pfeffer (at IAP), Jacobo Salvador (at UNPA, Argentina), Martín "el griego" Palopoli, Pablo Quiroz, and José Luis Hormaechea for their support and help in maintaining SIMONe Argentina. Open Access funding enabled and organized by Projekt DEAL.

References

Avsarkisov, V., Becker, E., & Renkwitz, T. (2022). Turbulent parameters in the middle atmosphere: Theoretical estimates deduced from a gravity-wave resolving general circulation model. *Journal of the Atmospheric Sciences*, *79*(4), 933–952. https://doi.org/10.1175/jas-d-21-0005.1

Becker, E. (2009). Sensitivity of the upper mesosphere to the Lorenz energy cycle of the troposphere. *Journal of the Atmospheric Sciences*, *66*(3), 647–666. https://doi.org/10.1175/2008jas2735.1

Becker, E. (2012). Dynamical control of the middle atmosphere. *Space Science Reviews*, *168*(1), 283–314. https://doi.org/10.1007/s11214-011-9841-5

Becker, E., & Vadas, S. L. (2018). Secondary gravity waves in the winter mesosphere: Results from a high-resolution global circulation model. *Journal of Geophysical Research: Atmospheres*, *123*(17), 2605–2627. https://doi.org/10.1002/2017jd027460

Becker, E., & Vadas, S. L. (2020). Explicit global simulation of gravity waves in the thermosphere. *Journal of Geophysical Research: Space Physics*, *125*(10), e2020JA028034. https://doi.org/10.1029/2020ja028034

Billant, P., & Chomaz, J.-M. (2001). Scaling analysis and simulation of strongly stratified turbulent flows. *Physics of Fluids*, *13*(6), 1645–1651. https://doi.org/10.1063/1.1369125

Brethouwer, G., Billant, P., Lindborg, E., & Chomaz, J.-M. (2007). Scaling analysis and simulation of strongly stratified turbulent flows. *Journal of Fluid Mechanics*, *585*, 343–368. https://doi.org/10.1017/s0022112007006854

Brune, S., & Becker, E. (2013). Indications of stratified turbulence in a mechanistic GCM. *Journal of the Atmospheric Sciences*, *70*(1), 231–247. https://doi.org/10.1175/jas-d-12-025.1

Callies, J., Ferrari, R., & Bühler, O. (2014). Transition from geostrophic turbulence to inertia–gravity waves in the atmospheric energy spectrum. *Proceedings of the National Academy of Sciences*, *111*(48), 17033–17038. https://doi.org/10.1073/pnas.1410772111

Caulfield, C. P. (2020). Open questions in turbulent stratified mixing: Do we even know what we do not know? *Physical Review Fluids*, *5*(11), 110518. https://doi.org/10.1103/physrevfluids.5.110518

Caulfield, C. P. (2021). Layering, instabilities, and mixing in turbulent stratified flows. *Annual Review of Fluid Mechanics*, *53*(1), 113–145. https://doi.org/10.1146/annurev-fluid-042320-100458

Chau, J. L., & Clahsen, M. (2019). Empirical phase calibration for multi-static specular meteor radars using a beam-forming approach and arbitrary interferometric configurations. *Radio Science*, *54*(1), 60–71. https://doi.org/10.1029/2018RS006741

Chau, J. L., Urco, J. M., Avsarkisov, V., Vierinen, J. P., Latteck, R., Hall, C. M., & Tsutsumi, M. (2020). Four-dimensional quantification of Kelvin-Helmholtz instabilities in the polar summer mesosphere using volumetric radar imaging. *Geophysical Research Letters*, *47*(1), e2019GL086081. https://doi.org/10.1029/2019gl086081

Chau, J. L., Urco, J. M., Vierinen, J., Harding, B. J., Clahsen, M., Pfeffer, N., et al. (2021). Multistatic specular meteor radar network in Peru: System description and initial results. *Earth and Space Science*, *8*(1), e2020EA001293. https://doi.org/10.1029/2020ea001293

Conte, J. F., Chau, J. L., Urco, J. M., Latteck, R., Vierinen, J., & Salvador, J. O. (2021). First studies of mesosphere and lower thermosphere dynamics using a multistatic specular meteor radar network over southern Patagonia. *Earth and Space Science*, *8*(2), e2020EA001356. https://doi.org/10.1029/2020EA001356

Davidson, P. (2013). *Turbulence in rotating, stratified and electrically conducting fluids*. Cambridge University Press.

Dewan, E. M. (1979). Stratospheric wave spectra resembling turbulence. *Science*, *204*(4395), 832–835. https://doi.org/10.1126/science.204.4395.832

Dewan, E. M., & Good, R. E. (1986). Saturation and the "universal" spectrum for vertical profiles of horizontal scalar winds in the atmosphere. *JGR Atmospheres*, *91*(D2), 2742–2748. https://doi.org/10.1029/jd091id02p02742

Falder, M., White, N. J., & Caulfield, C. P. (2016). Seismic imaging of rapid onset of stratified turbulence in the South Atlantic Ocean. *Journal of Physical Oceanography*, *46*(4), 1023–1044. https://doi.org/10.1175/jpo-d-15-0140.1

Falkovich, G. (1992). Inverse cascade and wave condensate in mesoscale atmospheric turbulence. *Physical Review Letters*, *69*(22), 3173–3176. https://doi.org/10.1103/physrevlett.69.3173

Gage, K. S. (1979). Evidence far a $k^{-5/3}$ law inertial range in mesoscale two-dimensional turbulence. *Journal of the Atmospheric Sciences*, *36*(10), 1950–1954. https://doi.org/10.1175/1520-0469(1979)036<1950:efalir>2.0.co;2

Gardner, C. (1994). Diffusive filtering theory of gravity wave spectra in the atmosphere. *JGR Atmospheres*, *99*(D10), 20601–20622. https://doi.org/10.1029/94jd00819

Ghosh, P., He, M., Latteck, R., Renkwitz, T., Avsarkisov, V., Zecha, M., & Chau, J. L. (2022). Characteristics of frequency-power spectra in the troposphere and lower stratosphere over Andøya (Norway) revealed by MAARSY. *Journal of Geophysical Research: Atmospheres*, *127*(13), e2021JD036343. https://doi.org/10.1029/2021jd036343

Holloway, G. (1988). The buoyancy flux from internal gravity wave breaking. *Dynamics of Atmospheres and Oceans*, *12*(2), 107–125. https://doi.org/10.1016/0377-0265(88)90021-8

Koshyk, J. N., Boville, B. A., Hamilton, K., Manzini, E., & Shibata, K. (1999). Kinetic energy spectrum of horizontal motions in middle-atmosphere models. *Journal of Geophysical Research*, *104*(D22), 27177–27190. https://doi.org/10.1029/1999jd900814

Li, Q., & Lindborg, E. (2018). Weakly or strongly nonlinear mesoscale dynamics close to the tropopause? *Journal of the Atmospheric Sciences*, *75*(4), 1215–1229. https://doi.org/10.1175/jas-d-17-0063.1

Lilly, D. K. (1983). Stratified turbulence and the mesoscale variability of the atmosphere. *Journal of the Atmospheric Sciences*, *40*(3), 749–761. https://doi.org/10.1175/1520-0469(1983)040<0749:statmv>2.0.co;2

Lindborg, E. (1999). Can the atmospheric kinetic energy spectrum be explained by two-dimensional turbulence? *Journal of Fluid Mechanics*, *388*, 259–288. https://doi.org/10.1017/s0022112099004851

Lindborg, E. (2006). The energy cascade in a strongly stratified fluid. *Journal of Fluid Mechanics*, *550*(1), 207–242. https://doi.org/10.1017/s0022112005008128

Lindzen, R. (1981). Turbulence and stress owing to gravity wave and tidal breakdown. *Journal of Geophysical Research*, *86*(C10), 9707–9714. https://doi.org/10.1029/jc086ic10p09707

Liu, H.-L. (2019). Quantifying gravity wave forcing using scale invariance. *Nature Communications*, *10*(1), 1–12. https://doi.org/10.1038/s41467-019-10527-z

Lübken, F.-J. (1999). Thermal structure of the Arctic summer mesosphere. *Journal of Geophysical Research*, *104*, 9135–9149.

McIntyre, M. (2000). Perspectives in fluid dynamics. In *On global-scale atmospheric circulations* (pp. 557–624). Cambridge University Press.

Nastrom, G. D., & Gage, K. S. (1985). A climatology of atmospheric wavenumber spectra of wind and temperature observed by commercial aircraft. *Journal of the Atmospheric Sciences*, *42*(9), 950–960. https://doi.org/10.1175/1520-0469(1985)042<0950:acoaws>2.0.co;2

Poblet, F. L., Chau, J. L., Conte, J. F., Avsarkisov, V., Vierinen, J., & Charuvil Asokan, H. (2022). Horizontal wavenumber spectra of vertical vorticity and horizontal divergence of mesoscale dynamics in the mesosphere and lower thermosphere using multistatic specular meteor radar observations. *Earth and Space Science*, *9*(9), e2021EA002201. https://doi.org/10.1029/2021ea002201

Poblet, F. L., Vierinen, J., Avsarkisov, V., Conte, J. F., Asokan, H. C., Jacobi, C., & Chau, J. L. (2023). Horizontal correlation functions of wind fluctuations in the mesosphere and lower thermosphere. *Journal of Geophysical Research: Atmospheres*, *128*(6), e2022JD038092. https://doi.org/10.1029/2022jd038092

Riley, J. J., & Lindborg, E. (2013). Ten chapters in turbulence. In *Recent progress in stratified turbulence* (pp. 269–317). Cambridge University Press.

Simmons, A. J., & Burridge, D. M. (1981). An energy and angular momentum conserving vertical finite-difference scheme and hybrid vertical coordinates. *Monthly Weather Review*, *109*(4), 758–766. https://doi.org/10.1002/2017JD027460

Smith, S., Fritts, D., & VanZandt, T. (1987). Evidence for a saturated spectrum of atmospheric gravity waves. *Journal of the Atmospheric Sciences*, *44*(10), 1404–1410. https://doi.org/10.1175/1520-0469(1987)044<1404:efasso>2.0.co;2

Smyth, W. D., & Moum, J. N. (2000). Anisotropy of turbulence in stably stratified mixing layers. *Physics of Fluids*, *12*(6), 1343–1362. https://doi.org/10.1063/1.870386

Tennekes, H. (1975). Eulerian and Lagrangian time microscales in isotropic turbulence. *Journal of Fluid Mechanics*, *67*(3), 561–567. https://doi.org/10.1017/s0022112075000468

Vadas, S. L., & Becker, E. (2018). Numerical modeling of the excitation, propagation, and dissipation of primary and secondary gravity waves during wintertime at McMurdo Station in the Antarctic. *Journal of Geophysical Research*, *123*(17), 9326–9369. https://doi.org/10.1029/2017jd027974

VanZandt, T. E. (1982). A universal spectrum of buoyancy waves in the atmosphere. *Geophysical Research Letters*, *9*(5), 575–578. https://doi.org/10.1029/gl009i005p00575

Weinstock, J. (1990). Saturated and unsaturated spectra of gravity waves and scale-dependent diffusion. *Journal of the Atmospheric Sciences*, *47*(18), 2211–2226. https://doi.org/10.1175/1520-0469(1990)047<2211:sausog>2.0.co;2

Weinstock, J. (1996). Spectra and a global source of gravity waves for the middle atmosphere. *Advances in Space Research*, *17*(11), 67–76. https://doi.org/10.1016/0273-1177(95)00731-s

Zhao, J., Chu, X., Chen, C., Lu, X., Fong, W., Yu, Z., et al. (2017). Lidar observations of stratospheric gravity waves from 2011 to 2015 at McMurdo (77.84°S, 166.69°E), Antarctica: 1. Vertical wavelengths, periods, and frequency and vertical wave number spectra. *Journal of Geophysical Research: Atmospheres*, *122*(10), 5041–5062. https://doi.org/10.1002/2016jd026368